

Dielectric slot-coupled half-Maxwell fisheye lens as octave-bandwidth beam expander for terahertz-range applications

Daniel Headland,^{*†} Andreas K. Klein,[‡] Masayuki Fujita,^{*†} and Tadao Nagatsuma,[†]

December 31, 2021

Abstract

We present a paradigm for integrated photonic devices based upon broadband slab-confined collimated beams that are launched with half-Maxwell fisheye lenses. Although it is challenging to match to the low-index focus of the lens whilst maintaining adequate field confinement for a well-defined point source, integrated dielectric slot waveguides prove highly suitable, yielding collimators of 90% efficiency and over one octave bandwidth. Terahertz technology will benefit from such broadband slab-confined beams to replace free-space optics, toward compact, mass-producible systems that do not require manual optical alignment. We present two prototype systems to demonstrate the versatility of this concept, namely a diagonally-set distributed Bragg reflector as frequency-division diplexer for terahertz communications, and an attenuated total reflection-based liquid sensor. Both are enabled by oblique in-slab reflections that are collected at a location other than the originating lens, which is not attainable using ordinary single-mode channel waveguides.

1 Introduction

A dielectric slab waveguide supports infinite in-plane propagating modes, and although this presents complexities in comparison to single-mode channel waveguides, there are also several advantages. The fundamental TE_0 slab-mode exhibits no cutoff or leakage at lower frequencies, and hence it is highly broadband and low-dispersion.¹ With in-slab beamforming techniques and integrated optics, this mode can propagate as a well-defined collimated beam.² The fact that these beams are free to propagate in in-plane directions allows for diagonally-set features to generate oblique reflections, and thereby direct the scattered radiation away from its originating direction. This is in contrast to channel waveguides, for which in-guide reflections always propagate back towards the source. Thus, dielectric slab waveguides present an effective means to separate forward- and backward-traveling waves in broadband. Furthermore, overlapping beams may be separated and collected independently if they propagate in distinct directions, as in the case of arrayed waveguide gratings.³

The planar half-Maxwell fisheye lens is a semicircular gradient-index (GRIN) optic that operates as a beam expander by interfacing a point source at the apex of its circumferential arc to a collimated beam that is projected normally from the bisecting line.^{4,5} As its focal length is half its diameter, a half-Maxwell fisheye lens is innately compact. This manner of GRIN lens is amenable to integrated photonics, as it may be implemented in a dielectric slab using effective medium techniques, i.e. as an array of subwavelength-pitch through-holes.^{2,6,7} If the slab is left unpatterned on the opposing side of the bisecting line, then the resulting structure is capable of both launching and receiving a slab-confined collimated beam. An integrated channel waveguide may interface with the lens' focus, but the particular choice of waveguide type is critical, as it must be matched to the relatively low index at the lens' circumference whilst avoiding delocalization of modal fields into the surrounding space.⁸ Previously, we have employed photonic crystal waveguides for this purpose,² but it was found that the photonic crystal adjacent to a receiving lens' focus strongly reflected un-collected stray fields back into the slab, leading to undesired interference. Here, we show that a dielectric slot waveguide, which confines radiation within a narrow air gap,⁹ is a highly effective solution. The result is an efficient slab-mode beam collimator with over one octave bandwidth, outperforming integrated beam expanders that are based upon optimized-profile waveguide tapers.^{10,11}

Our experimental investigation targets the terahertz range, which will benefit from this integrated optics paradigm. Terahertz waves hold potential for attractive applications such as imaging,^{12,13} spectroscopy,^{14,15} and communications.^{16,17} However, the majority of reported demonstrations incorporate bulky free-space optics that require manual assembly and precise alignment, reducing the viable scope of real-world applications. As an alternative, we wish to monolithically integrate all optics of a given system within a single high-resistivity float-zone intrinsic silicon wafer, and fabricate them together in their appropriate alignment. In this way, we devise two practical use-cases; a distributed Bragg reflector (DBR)-based broadband frequency-division diplexer for terahertz communications applications, and an attenuated total internal reflection (ATR)-based terahertz liquid sensor.

^{*}Corresponding author

[†]Graduate School of Engineering Science, Osaka University, Osaka 560-8531, Japan

[‡]Department of Optoelectronics, University Duisburg-Essen, 47057 Duisburg, Germany

2 Results

2.1 Lens design

A Maxwell fisheye lens is described by a radially symmetrical distribution of refractive index given by,¹⁸

$$n(r) = \frac{n(0)}{1 + \frac{r}{r_{\max}}^2}, \quad (1)$$

where r_{\max} is the radius of the optic and $n(0)$ is the peak refractive index that is found at the center of the lens. The index distribution must vary continuously between $n(0)$ and half this value, as $n(r_{\max}) = n(0)/2$, and hence it is a requirement of the GRIN medium that the achievable range of refractive index must span a two-to-one ratio. In this work, an effective medium composed of a triangular lattice of subwavelength through-holes in a silicon slab provides engineerable effective index that is mediated by hole diameter.^{2, 7, 19–21} Our investigation targets frequencies in the vicinity of 300 GHz, for which hole pitch of $\sim 88 \mu\text{m}$ is appropriate. In consideration of realistic fabrication constraints, the minimum viable hole diameter is $\sim 20 \mu\text{m}$, and this informs our selection of $n(0) = 2.9$. Having defined this parameter, Eq 1 provides a complete description of index distribution for the TE_0 slab mode that is employed in the present work. This translates¹ to a bulk refractive index that varies from ~ 3.3 in the lens center to ~ 1.8 at the edge, corresponding to hole diameters $\sim 20 \mu\text{m}$ and $\sim 75 \mu\text{m}$, respectively. The design procedure to determine the required layout of hole sizes in the lens body is described in detail in the Methods section.

The optic that is the main subject of this work is illustrated in Fig. 1. A Maxwell fisheye lens is bisected in order to yield a half-Maxwell fisheye lens, and an unpatterned silicon slab is attached to the bisecting line. An effective medium-clad dielectric channel waveguide^{19, 21} interfaces with the focus that is situated at the apex of the semicircular arc, and terahertz waves are provided via an external hollow waveguide. A 2.8 mm linear-tapered spike at the termination of the channel waveguide is inserted into the hollow metallic waveguide in order to perform broadband index matching, as is commonplace for experimental characterization of all-dielectric terahertz waveguide devices.^{2, 7, 19–25}

The feeding structure that is employed to interface to the integrated optic is of critical importance, as it must provide index matching whilst simultaneously confining terahertz waves into a narrow point source. For the lens, the focus may be represented as a moderately low-index dielectric slab region, as shown in Fig. 2(a). For the channel waveguide, it can be seen in the inset to Fig. 1 that a narrow slot is etched into its termination, thereby forming a dielectric slot waveguide.⁹ This choice can be understood by comparison with more conventional dielectric waveguides, as shown in Figs. 2(b),(c), alongside a dielectric slot waveguide in Fig. 2(d). Cladding is omitted for simplicity and clarity in this discussion. Simulated modal field distributions of candidate channel waveguides are given in Figs. 2(e)–(m), and Fig. 2(n) shows their dispersion relations along with that of the slab waveguide, where it is noted that index less than unity corresponds to leaky modes that exhibit progressive loss via radiation to free-space. It can be seen from Fig. 2(n) that the

modal index of the narrow dielectric waveguide given in Fig. 2(b) is sufficiently low for reasonable index matching to the slab, however Figs. 2(e) and (h) indicate that this is due to de-localization of modal fields into the surrounding space, which increases at lower frequencies. An undesired consequence of this is that the fields that are supplied by this waveguide are a poor match to the point source to which the half-Maxwell fisheye lens is suited, and hence the resulting slab-mode beam will be of low quality. On the other hand, Figs. 2(f) and (i) show that the wider dielectric waveguide can achieve stronger field confinement, but this comes at the cost of greatly increased modal index, as observed in Fig. 2(n), and this negatively impacts matching. Put simply, the dielectric waveguide presents an unwelcome trade-off that is mediated by waveguide width; we may either achieve index matching or field confinement, but we cannot obtain both simultaneously.

The dielectric slot waveguide that is illustrated in Fig. 2(d) confines terahertz waves strongly within an airgap, as shown in Figs. 2(g)–(j). As a consequence, modal fields primarily occupy a low-index material, and hence the overall effective modal index is reasonably low, as shown in Fig. 2(n). Furthermore, the dielectric slot waveguide is of lower dispersion than the narrow dielectric waveguide, as its modal field distribution varies less with respect to change in frequency. For these reasons, the dielectric slot waveguide is well suited to feed the integrated half-Maxwell fisheye lens.

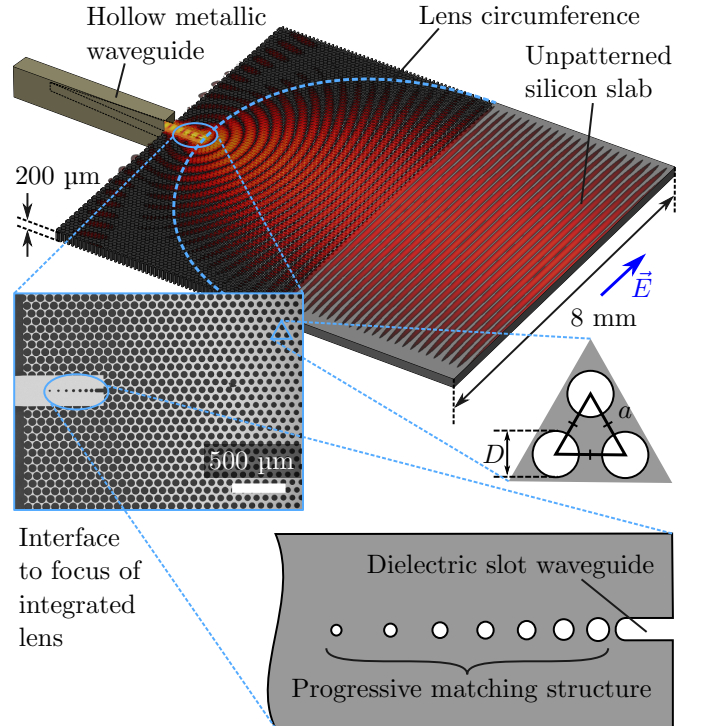


Figure 1: Integrated half-Maxwell fisheye lens-based slab-mode beam launcher, showing a schematic diagram of the lens itself, coupling terahertz waves from an external hollow metallic waveguide to an un-patterned dielectric slab. An inset micrograph shows the detail of the feed structure that interfaces to the lens’ circumference, including a slot waveguide that is matched to a wide channel waveguide via a progressive hole-array structure. A single period of a triangular lattice of cylindrical holes is shown.

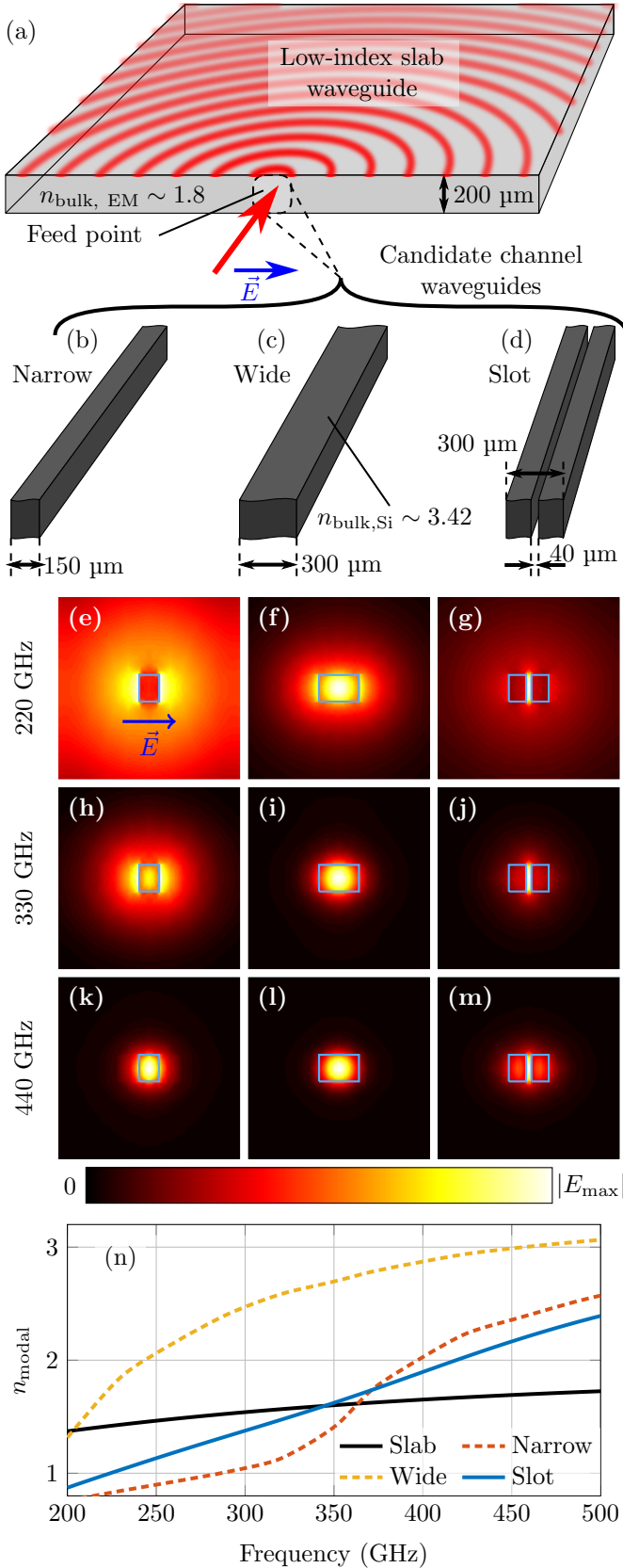


Figure 2: Interface to lens, showing abstract, schematic representation of (a) the low-index slab waveguide at lens' feed point, and (b)–(c) candidate channel waveguides, as well as (e)–(m) electric field magnitude distributions of fundamental propagating modes of each such channel waveguide, given in linear scale and normalized to their respective maxima, and (n) modal indices. In all cases, we consider the fundamental TE mode exclusively.

Having selected the appropriate manner of feeding structure for the integrated half-Maxwell fisheye lens-based slab-mode beam launcher, we may proceed with the details of the feed design. Although we employ a hollow metallic waveguide to provide an interface to the external world, it is unsuited to launch a dielectric slot mode directly, and hence a 306 μm -wide dielectric waveguide is employed as an interface. A progressive hole-matching structure serves as a compact transition between the dielectric waveguide and dielectric slot modes. There are seven holes, of diameter varying from 20 μm to 35 μm , and hole separation is from 63 μm to 13 μm . The slot itself is 37 μm -wide and 70 μm -long. This final design is shown in Fig. 1.

In order to experimentally verify the existence of the slab-mode beam, we devise a sample that consists of two lenses that face each other across a 1 cm-long slab region as a simple transmission configuration. A source is coupled to one of the lenses and a detector is coupled to the other, and hence successful transfer of terahertz power through the sample constitutes evidence for the existence of the slab-mode beam. This experiment is shown in the photograph in Fig. 3(a). The coupling efficiency of a single lens is extracted from the measured transmission, and is given in Fig. 3(b). It can be seen that the 3-dB bandwidth of the optic is not encountered across the measurable range. Fortunately, the frequency range of full-wave simulations is less constrained, and hence simulations facilitate a broader-bandwidth investigation. Such techniques also provide insight into lens matching performance and field distributions, which are not measurable with our available equipment. Simulated results given in Fig. 3(b) show that the lower-frequency cutoff is encountered at ~ 216 GHz, and above this frequency, reflection magnitude is below -10 dB. Overall bandwidth exceeds one octave, and peak transmission efficiency is $\sim 90\%$, but it is noted that this performance corresponds to ideal alignment with the hollow waveguide. Simulated field distributions are given in Figs. 3(c)–(e), where it can be seen that a high-quality collimated beam is produced over a broad bandwidth. Insight is sought into the impact of the dielectric slot waveguide and associated matching structure, and hence these components are removed, leaving a wide dielectric waveguide, and reflection response is re-calculated via full-wave simulation. This scenario is illustrated inset to Fig. 3(b), and it can be seen that reflection magnitude has indeed increased to ~ -10 dB across a broad bandwidth.

2.2 Prototype systems and applications

Having completed the design of the integrated terahertz lens in Section 2.1, the aim of the present section is to develop prototype integrated optical systems in order to demonstrate the practical utility of the emerging terahertz slab-mode beam paradigm. A range of passive functional optical components may be implemented directly in the slab using an arrangement of through-holes, and integrated beam splitters are one such possibility. To this end, a stripe of effective medium can produce an index step, and thereby generate reflections of magnitude that is dependent upon air filling-factor and the width of the stripe. Crucially, the use of freely propagating beams al-

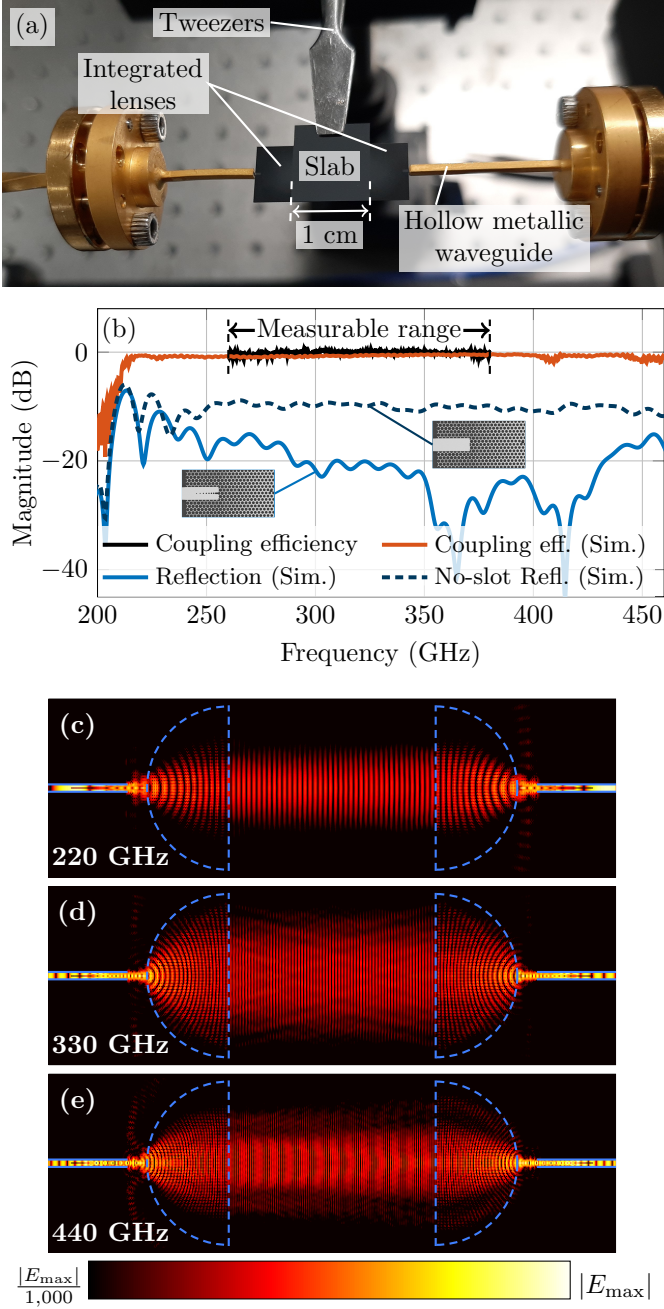


Figure 3: Evaluation of the half-Maxwell fisheye lens' performance by means of a two-lens sample, which is shown undergoing experimental characterization in (a). (b) Coupling efficiency of a single lens, as well as simulated matching performance as represented by reflection magnitude, both with and without the slot waveguide and associated matching structure, and (c)–(e) simulated field magnitude distributions of two-lens structure at several frequencies of interest, where each is shown in logarithmic scale, and normalized to its respective maximum.

lows this stripe to be set obliquely, such that the reflected radiation may be directed to a location other than that of its originating lens. Thus, the slab-mode beam paradigm can separate backward- and forwards-traveling waves in a manner that linear channel waveguides cannot.

It is well understood that periodic alternation of a medium's dielectric properties can produce frequency-dependent transmission and reflection.^{26,27} This concept may be implemented in a slab waveguide by means of an

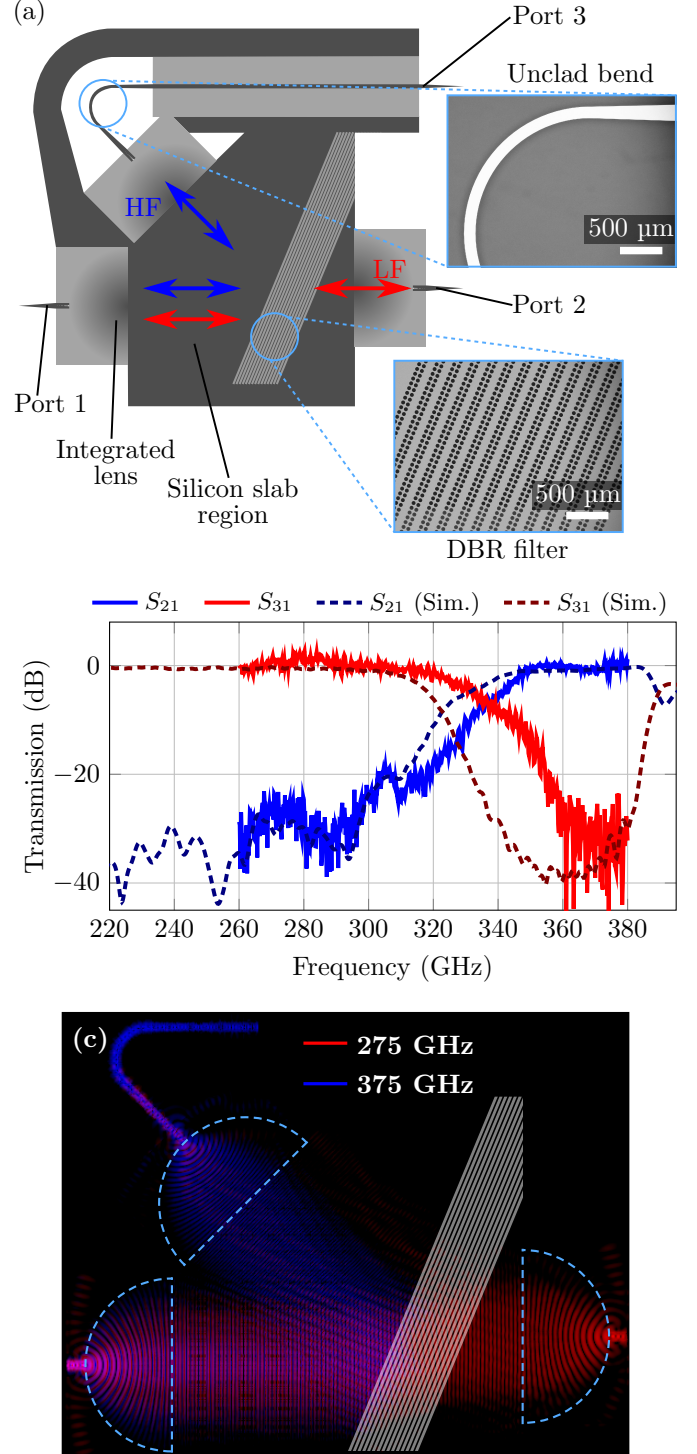


Figure 4: Integrated DBR-based frequency diplexer, showing (a) schematic, with inset micrographs, (b) transmission magnitude between each pair of ports, and (c) simulated field magnitude distributions at two frequencies of interest, in false-color representation. Each field plot is normalized to its own maximum, and is given in logarithmic scale with 30 dB dynamic range.

array of stripes of effective medium, thereby realizing a DBR or dichroic beam splitter, which serves as an optical filter in the present work. As illustrated in Fig. 4(a), such a structure may be integrated directly with a three-lens setup in order to realize an all-dielectric broadband frequency-division diplexer. The DBR optical filter is set at a 22.5° angle, in order to achieve 45° separation between the originating lens and that which collects the fil-

ter's stopband. The filter is optimized for cross-over at ~ 320 GHz, i.e. the center of our measurable range, and is composed of 47 μm -diameter cylindrical through-holes in a 64 μm -period square lattice. Each stripe constitutes two rows of through-holes, and the periodic separation between adjacent stripes is 203 μm . It is noted that, although this microstructure is effective medium, a single stripe contains too few rows of holes to be accurately modeled using effective-medium theory, for which approximate local uniformity is required. Thus, it is not possible to provide a meaningful value for effective refractive index. There are fifteen stripes in total, and a micrograph of the integrated filter is shown inset to Fig. 4(a). The lens that is intended to collect the passband is raised by 1.3 mm with respect to the originating lens, in order to account for refraction during transit through the lower-effective index portions of the optical filter. A 135° unclad bend²⁰ is employed to re-route the reflected stopband following transit through its associated lens, such that it exits the sample parallel to the passband port in order to facilitate ease of probing. In addition to this, the bend structure's width is narrowed to 145 μm via linear tapers in order to radiate low frequencies and improve out-of-band rejection. The principle of operation of this bend-as-filter structure is that narrow waveguides exhibit progressively weaker field confinement with respect to decrease in operation frequency, as shown in Fig. 2(e),(h), and (k). A micrograph of the bend is given as inset to Fig. 4(a).

The measured transmission of the integrated DBR-based terahertz frequency-division diplexer is given in Fig. 4(c), along with simulated response. It can be seen that efficient broadband frequency-splitting is indeed achieved, and hence the intended functionality of this device is validated. However, the crossover-point has shifted upwards in frequency by ~ 18 GHz. We ascribe this to the employed wafer thickness being lower than its nominal specification, leading to changes in the dispersion profile of the slab and effective medium that comprise the integrated filter. A thinner wafer will also produce over-etching of the small holes of the filter, which reduces the effective index of the stripes, and increases the frequency of the wavelength that corresponds to a stopband period. False-color field plots from the full-wave simulations are given in Fig. 4(c), showing the separation of the slab-confined beam into two distinct frequencies by the integrated DBR-based optical filter.

The primary intended application of the frequency-division diplexer is high-volume terahertz-range communications,¹⁶ and hence it is desirable to validate its applicability thereto. To this end, on-off-keying-modulated terahertz waves are generated using a uni-traveling carrier photodiode (UTC-PD), conveyed through the integrated diplexer, and subsequently detected by a Schottky-barrier diode (SBD). A photograph of this experiment is included in Fig. 5(a). Both channels of the diplexer are employed, and a range of terahertz carrier frequencies within their respective transmission bandwidths is utilized. In each case, the highest data rate is found that abides a given maximum measured bit-error rate (BER) within a finite 30-second timespan. The three chosen maximum BER values are "error-free," for which no errors are counted (although finite errors would be counted if the timespan were extended indefinitely), $\text{BER} < 1 \times 10^{-10}$, and

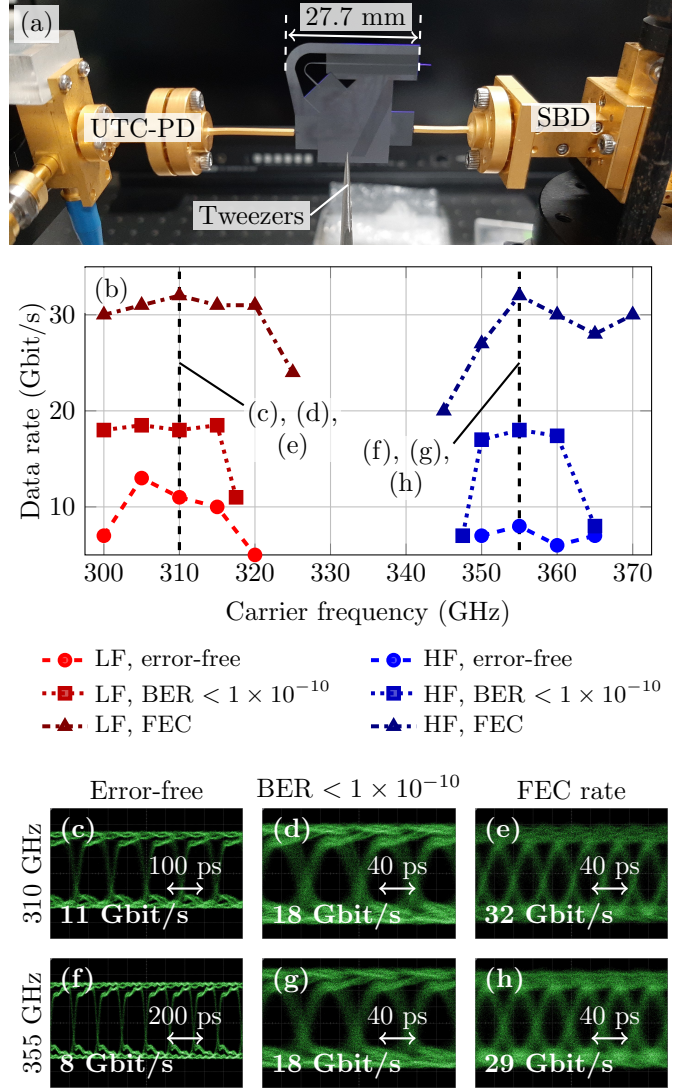


Figure 5: Demonstration of terahertz communications, showing (a) photograph of experiment, (b) achievable data rates at three different maximum bit-error rates, for a variety of carrier frequencies, and (c)–(h) eye diagrams.

“forward error-correction (FEC)”-achievable rate, which is 2×10^{-3} .²⁸ The results of this experiment are given in Fig. 5(b). It can be seen that data rates of between ~ 8 Gbit/s and ~ 30 Gbit/s are achievable, where higher permitted BER is associated with increased achievable data rates, as expected. Additional to that, performance is observed to decrease as carrier frequency approaches the cross-over frequency of the device. Eye diagrams at 310 GHz and 355 GHz are given in Fig. 5(c)–(h), and a clearly-open “eye” is visible in each case.

Aside from broadband communications, terahertz waves have also been nominated for applications in spectroscopy^{14,15} and liquid sensing.^{23,29} To support the integration of systems of this sort, it is possible to define sensing areas in the silicon slab medium where the slab-mode interfaces with the a given analyte in order to probe its properties. A simple example of a sensing area is a straight edge. If a terahertz slab-mode beam is impinged upon this interface at an oblique angle, then total internal reflection (TIR) will occur due to the large index contrast between air and silicon. On the other hand, if a liquid substance of greater-than-unity refractive index is introduced

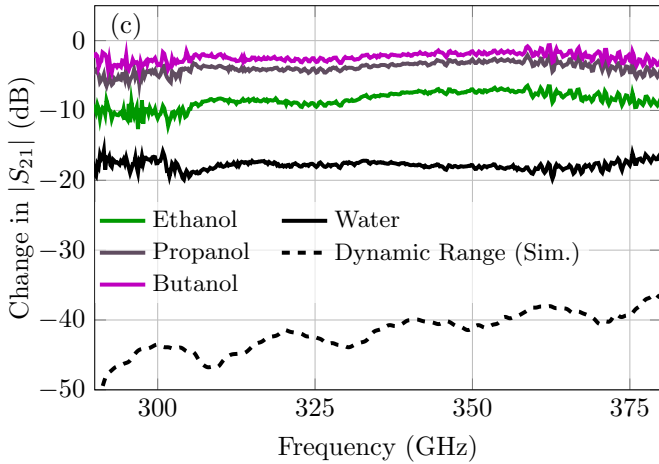
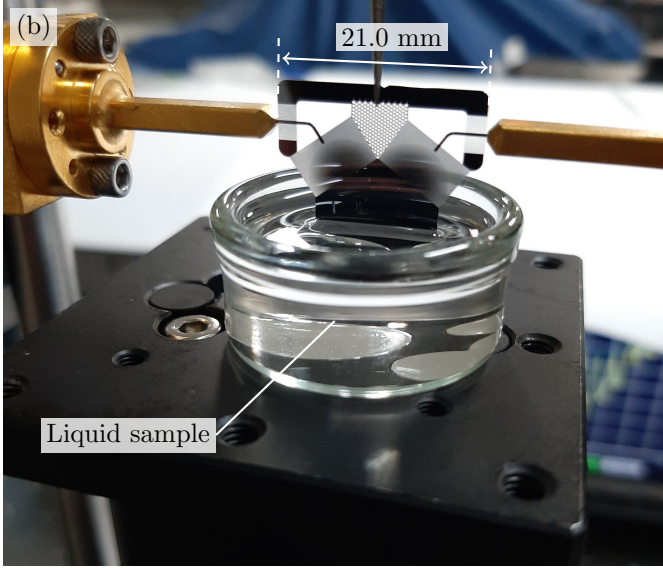
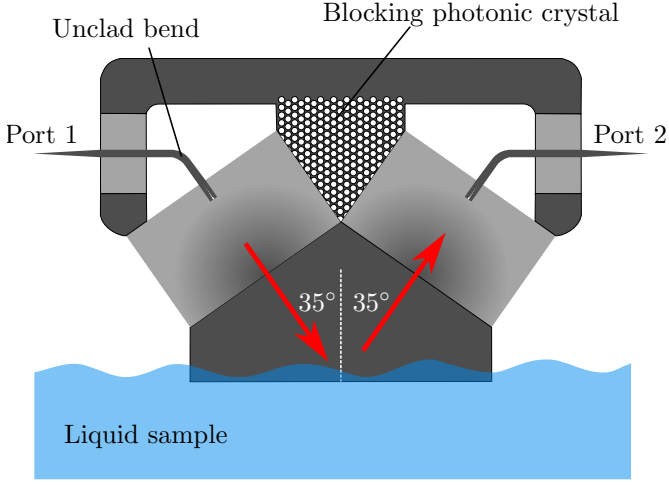


Figure 6: Integrated ATR-based dip sensor, showing (a) schematic representation, (b) photograph of liquid sensing experiment, and (c) the change, or deviation in transmission magnitude due to the presence of a variety of polar liquids at the sensing area, as compared to the case in which only air is present.

to the sensing area then TIR may be inhibited, resulting in attenuation of the reflected wave. Thus, it is possible to sense the presence and properties of that liquid by measuring the attenuation of the reflected beam, thereby realizing ATR-based sensing.³⁰ An integrated slab-mode device to realize terahertz ATR is illustrated in Fig. 6(a). Unclad

bends²⁰ are employed in order to feed the integrated lenses at the desired angle, whilst maintaining ports that are co-linear and anti-parallel for ease of probing. As these two ports face each other directly, broadband photonic crystal medium is included in the space between them as a precaution in order to inhibit undesired direct transmission, whilst providing physical support. An angle of incidence of 35° is chosen in order to maximize the dynamic range (DR) between the refractive index of water and unity.

The integrated ATR sample is fabricated and deployed as a terahertz dip-sensor, as shown in the photograph in Fig. 6(b). We employ several common polar solvents, namely distilled water and alcohols of different chain length, and determine the change in transmission magnitude between the two ports due to the presence of the liquid. The results of this experiment are given in Fig. 6(c), and it can be seen that all of the polar solvents employed are clearly distinguishable by their respective reflection. The measured DR of the liquid sensor is 18–20 dB, corresponding to the case of distilled water, which exhibited the largest overall loss. The theoretical maximum DR of the sensor is limited by undesired transmission of stray terahertz power, which does not interact with the sensing area, between Ports 1 and 2. This is investigated in simulation by absorbing all fields that are incident upon the sensing area, and the results given in Fig. 6(c) show that theoretical maximum DR is greater than 37 dB across the measured bandwidth.

As for the alcohols, a clear tendency of increasing reflection with respect to decrease in refractive index can be observed. This is to be expected as alcohols of greater chain length exhibit increased index contrast to the silicon. Propanol and butanol are distinguishable despite the small difference in relative permittivity ($\Delta\epsilon'$ and $\Delta\epsilon'' < 0.1$), thereby demonstrating the high sensitivity of the liquid sensor.²⁹

3 Discussion

We have realized an efficient dielectric slab-mode beam launcher with bandwidth over one octave. To support this, we have shown that a dielectric slot waveguide serves as an effective means to interface a low-index slab waveguide to a dielectric channel waveguide, and we deploy this solution to feed an integrated half-Maxwell fisheye lens. It is noted that a multitude of other GRIN optics may also benefit from this technique, including Luneburg and Eaton lenses^{31–33} across the electromagnetic spectrum. Aside from integrated lenses, it is noted that quasi-conformal transformation optics may also be implemented in gradient-index effective medium,^{34,35} and hence the dielectric slot waveguide may serve to directly feed a broad range of advanced transformation-optics devices.

One limitation of the dielectric slot waveguide feed is its polarization. We have employed the TE polarization (i.e. \vec{E} -field is surface-parallel) exclusively in this work. Although the TM polarization (i.e. \vec{E} -field is surface-normal) is also supported by a dielectric slot waveguide, its modal fields are not confined within the airgap, and so it does not exhibit comparably narrow confinement, and its dispersion relation is quite different. Thus, the slab-mode beam launcher that is the main subject of this

work will not support polarization-diverse applications. Another potential limitation is the sensitivity of micro-scale hole lattice structures to fabrication errors and variation in thickness between silicon wafers, as in the case of the DBR-based optical filter, for which the crossover frequency was shifted upwards by ~ 18 GHz. In order for future systems of this sort to be commercially viable, it will be necessary to develop optical filter designs that are more robust to tolerances, or to lay out the photolithographic mask in such a way that compensates for anticipated over-etching. Nevertheless, the frequency-division diplexer serves as a useful proof-of-concept, and its applicability to terahertz-range communications applications was demonstrated.

We wish to remark that effective medium techniques are not the sole viable means to realize GRIN terahertz optics, as the dispersion of a parallel-plate metallic waveguide may also serve to realize engineerable refractive index that is mediated by plate separation, and this has been demonstrated for Luneburg and Maxwell-fisheye lenses.^{36–38} That said, such devices exhibit Ohmic loss, and have no potential for integration. It is also noted that, although dielectric slot waveguides have previously been studied in the terahertz range,^{39–41} they have never been employed to directly feed optics at any frequency range.

The capacity to efficiently launch a terahertz slab-mode beam in broadband opens the door to realize diverse integrated terahertz optical systems. In contrast to devices that depend upon free-space beams, integrated systems will be considerably more compact, and will not require manual assembly and alignment of individual optics. Functional components, sensing areas, and other interfaces may be implemented directly in microstructured silicon. We have presented two integrated devices as concrete examples of viable usage cases—a DBR-based frequency-division diplexer and an ATR-based liquid sensor—both of which operate in broadband. It is likely that many other terahertz systems may be implemented in this way, to support a plethora of diverse applications of terahertz waves. Furthermore, terahertz technology will not be the sole beneficiary of broadband slab-mode beam launchers, as these passive, all-dielectric structures may be implemented across the electromagnetic spectrum, and are amenable to nanophotonics in particular.^{34,35} For instance, quantum-mechanical photonic technologies frequently rely upon oblique reflections of individual photons from free-space beam splitters.^{42,43} Slab-mode techniques represent a possibility to directly implement such techniques in a broadband integrated platform.

All of the structures presented in this work are implemented using through-holes in a silicon slab exclusively. This is a deliberate choice for the sake of simplicity, as only a single-mask etch process is required. On the other hand, the scope of terahertz applications would likely be expanded considerably by patterning a metal top layer, incorporating phase-change materials,⁴⁴ or by doping of the silicon itself. Hybrid integration with active terahertz devices also presents an opportunity to incorporate active terahertz devices,^{45,46} thereby rendering the hollow-metallic-waveguide interface obsolete, and reducing systems size further.

4 Materials and Methods

4.1 Model generation

4.1.1 Arrangement of through-holes in the lens

The half-Maxwell fisheye lens enjoys a closed-form design procedure, which we have previously presented.² Firstly, it is noted that radiation propagates within the lens as a mildly-dispersive TE_m slab-mode, and hence Eq. 1 is a description of slab-mode index, $n_{\text{slab},m}$. This must be translated into the refractive index of a bulk material, n_{eff} , for which a description of the dispersion relation of the slab waveguide is required,¹

$$\tan^2 \left\{ \frac{t}{2} \sqrt{(n_{\text{eff}} k_0)^2 - (k_0 n_{\text{slab},m})^2} - \frac{m\pi}{2} \right\} = \frac{(k_0 n_{\text{slab},m})^2 - k_0^2}{(n_{\text{eff}} k_0)^2 - (k_0 n_{\text{slab},m})^2}, \quad (2)$$

where k_0 is free-space wavenumber and t is dielectric slab thickness, which is equal to $200 \mu\text{m}$ in this work. The fundamental TE mode is employed in the present work, and hence $m = 0$. Solving this transcendental equation yields the required distribution of bulk effective index, n_{eff} , as a function of radial position within the lens body. Finally, this is converted to a layout of hole diameters by means of the Maxwell Garnett effective medium approximation,⁴⁷

$$n_{\text{eff}}^2 = \epsilon_{\text{Si}} \frac{(1 + \epsilon_{\text{Si}}) + (1 - \epsilon_{\text{Si}})\zeta}{(1 + \epsilon_{\text{Si}}) - (1 - \epsilon_{\text{Si}})\zeta}, \quad (3)$$

where ζ is the volumetric air filling-factor, which is calculated using the equilateral triangular hole-lattice geometry shown in Fig. 1,

$$\zeta = \left(\frac{D}{a} \right)^2 \frac{\pi}{2\sqrt{3}}. \quad (4)$$

4.1.2 Through-holes to clad channel waveguides

Following the example of Refs. 19,21, we clad the channel waveguide with effective medium that is as low-index as possible, and as a consequence, we wish to employ maximum viable hole diameter. In order to maintain structural robustness, we employ a minimum distance of $10 \mu\text{m}$ between adjacent holes. The hole lattice that comprises the lens itself is simply extended to form the cladding of the channel waveguide, and hence the two regions of effective medium share a common hole pitch. Thus, the diameter of the waveguide-cladding air holes is $78 \mu\text{m}$.

Semicircular holes make direct contact with the sides of the channel waveguide as a precaution against spatial index modulation along the propagation direction, which may cause undesired Bragg mirror effects at higher frequencies,²⁵ and thereby reduce bandwidth. This necessitates that the ratio of waveguide width to $\frac{a\sqrt{3}}{2}$ must be an integer, in order that both edges of the waveguide bisect a row of holes. This is ensured by making the hole pitch dependent upon waveguide width, and scripting the generation of the layout of holes in the lens body to update automatically in response to parametric adjustment of waveguide width. This manner of interconnected, parametric model generation facilitates convenient optimization.

4.2 Simulation

All simulations are performed using the commercially available CST Studio Suite electromagnetic full-wave simulation software package.

4.2.1 Full-wave simulation model

The frequency-domain mode solver of CST Studio Suite is employed to determine the modal field distributions and dispersion relations that are given in Fig. 2(e)–(n). Symmetry planes are employed in order to ensure that the displayed fundamental mode is of the desired polarization.

The simulation results given in Figs. 3(b)–(e) and 4(b),(c) are generated with the time-domain solver of CST Studio Suite, which employs the finite integral technique. In the reflection-magnitude results given in Fig. 3(b), a single-lens model is employed, and the outgoing beam is simply discarded by attaching the slab-region to an absorbing boundary. In this way, the reflections that are generated within the slab-mode beam launcher structure are essentially isolated, and the impact of features within the slab, as well as output coupling, are neglected.

In the case of the simulations of the DBR-based frequency-division diplexer that is given in Fig. 4(b),(c), some approximations are made in order to reduce the electrically-large calculation domain to a practical, manageable scope. The hole-lattice arrays that comprise the lenses themselves are replaced with a set of concentric semi-annular rings of bulk refractive index such that the TE_0 slab-mode index distribution corresponds to Eq. 1. Furthermore, the channel waveguide that conveys the DBR filter’s stopband to Port 3 is shortened, so as to reduce overall pulse-propagation time through the model.

For the liquid sensor that is presented in Fig. 6, the undesired direct transmission between Ports 1 and 2 is determined by placing an absorbing boundary at the surface of the sensing area. In this way, any field that would ordinarily interact with the analyte is removed from the calculation domain. The simulated transmission is normalized against that of a simulation in which the sensing area is in contact with air, and the results are presented in Fig. 6(c).

4.2.2 Optimization of microstructures

Optimization of microstructures such as the slot-waveguide feed and progressive matching structure shown in Fig. 2, as well as the DBR-based filter shown in Fig. 4(a), is performed manually. This consists of a repeated cycle of full-wave simulation, subjective appraisal of the quality of field distributions and S -parameters, and adjustment of the physical parameters that define the geometry of the structure in question. No automated optimization algorithm was employed. The reason for this choice is that the devices that are presented in this work are electrically large, and require a fine mesh for accurate representation of effective medium structures. As a consequence, simulation time can span several days. The amount of time that is required for manual adjustment by the designer is therefore insignificant compared to the overall simulation time, and hence there the usage of automation does not present an advantage in terms of time-

efficiency. This is because all optimization algorithms require a large number of simulations in order to produce a final design, whereas an experienced user is capable of making educated choices in each simulation step.

4.3 Experimental methods

4.3.1 Fabrication

All silicon devices are fabricated using deep-reactive ion etching (DRIE), which employs a single photolithographic mask. Several devices are etched concurrently from a single 200 μm -thick, 10 cm-diameter high-resistivity float-zone intrinsic silicon wafer.

4.3.2 Handling

Silicon samples are handled using ordinary tweezers that make contact with unpatterned portions of the device that serve no electromagnetic purpose. When the sample is secured for probing, the tweezers that bear the sample are manually clamped into a vice.

4.3.3 Characterization of transmission magnitude

Terahertz waves are generated electronically, via up-conversion of a millimeter-wave signal with a $\times 9$ multiplier, and then output by a hollow metallic waveguide of rectangular internal dimensions $711 \times 356 \mu\text{m}$ (i.e. WR-2.8). This terahertz power is conveyed to the silicon structures reported in this work by means of a 2.8 mm-long linear-tapered spike that provides broadband index-matching, and is inserted directly into the hollow metallic waveguide. Alignment between these two components is performed with micrometer-controlled stages. Following transit through the silicon device, the terahertz waves are collected by a second hollow metallic waveguide, and are demodulated via a mixer that is connected to a $\times 36$ multiplier, which up-converts the microwave-range local oscillator signal of a spectrum analyzer. As a result, received terahertz power is viewed as a function of frequency in the readout of the spectrum analyzer.

Normalization by a reference measurement is required in order to convert received power into transmission magnitude. In the case of the coupling efficiency that is given in Fig. 3(b), a back-to-back measurement with the hollow waveguides coupled directly together (not shown) serves as reference. Thereafter, the negative decibel-value transmission efficiency is halved in order to estimate the coupling efficiency of a single lens. For the transmission of the DBR-based beam-splitter that is presented in Fig. 4(b), the two-lens sample shown in Fig. 3(a) is an appropriate reference measurement, as it facilitates isolation of the response of the optical filter itself. Finally, the liquid-sensing results given in Fig. 6(c) are normalized against the transmission response of the same device with the liquid removed. Additional reference measurements are taken between individual liquid-sensing experiments, in order to verify that there is no undesired residue on the sensing area that may obfuscate the results of subsequent tests.

4.3.4 Terahertz-range communications

In order to support the demonstration of terahertz communications that is shown in Fig. 5, a UTC-PD photomixer is excited with an on-off-keying-modulated two-color infrared laser signal for which the beat frequency corresponds to the desired output terahertz frequency. The resultant down-conversion produces terahertz waves that inherit the amplitude modulation of the optical signal. This terahertz power is accessed via a hollow metallic waveguide, which is coupled to Port 1 of the DBR-based frequency-division diplexer. Following transit through the silicon device, the modulated terahertz waves are collected at either Port 2 or 3, and are input to an SBD-based detector, where they are converted directly to baseband via envelope detection. The demodulated bitstream is then amplified, clipped, and conveyed to both a bit error-rate tester and an oscilloscope simultaneously. The former serves to evaluate bit error-rate in real-time, and the latter displays the downconverted eye diagram.

The BER value corresponding to the FEC limit is selected based upon ITU-T recommendation G.975.1,²⁸ which suggests that, for 7% coding overhead, a pre-correction BER of 2×10^{-3} serves as an upper-bound. Above this BER value, error-correction is of limited utility to improve overall channel quality.

4.3.5 Liquid handling

All liquid chemicals are used as-delivered, and with the purity that is supplied by the manufacturer. Each liquid analyte is poured into an individual small glass petri-dish, to avoid cross-contamination. The petri-dish is placed upon a vertical translation stage, such that it may be brought into contact with the ATR-based liquid sensor without moving the device itself. This is necessary to maintain alignment with the hollow waveguides with which it is probed, with the aim being that measurements in the presence of liquids are comparable with those without, for normalization purposes. Following probing, the stage bearing the sample is lowered, the petri-dish is removed, and the liquid is discarded.

Acknowledgments

The authors wish to acknowledge support from the following grants: Core Research for Evolutional Science and Technology (CREST) program, Japan Science and Technology Agency (JST) (Grant No. JPMJCR1534); Grant-in-Aid for Scientific Research, the Ministry of Education, Culture, Sports, Science and Technology of Japan (Grant No. 20H01064); the Deutsche Forschungsgemeinschaft (DFG, German Research Foundation), Project ID ID287022738 TRR 196 (Project C06); the H2020-MSCA-ITN project TERAOPTICS- GA No. 956857.

References

- [1] Saleh, B. E. & Teich, M. C. *Fundamentals of photonics* (John Wiley & sons, 2019).
- [2] Headland, D., Fujita, M. & Nagatsuma, T. Half-Maxwell fish-eye lens with photonic crystal waveguide for the integration of terahertz optics. *Opt. Express* **28**, 2366–2380 (2020).
- [3] Takahashi, H., Hibino, Y. & Nishi, I. Polarization-insensitive arrayed-waveguide grating wavelength multiplexer on silicon. *Opt. Lett.* **17**, 499–501 (1992).
- [4] Lawrence, G. & Hwang, S.-H. Beam propagation in gradient refractive-index media. *Appl. Opt.* **31**, 5201–5210 (1992).
- [5] Fuchs, B. *et al.* Comparative design and analysis of Luneburg and half Maxwell fish-eye lens antennas. *IEEE Trans. Antennas Propag.* **56**, 3058–3062 (2008).
- [6] Hunt, J. *et al.* Planar, flattened Luneburg lens at infrared wavelengths. *Opt. Express* **20**, 1706–1713 (2012).
- [7] Headland, D., Withayachumnankul, W., Yamada, R., Fujita, M. & Nagatsuma, T. Terahertz multi-beam antenna using photonic crystal waveguide and Luneburg lens. *APL Photonics* **3**, 126105 (2018).
- [8] Almeida, V. R., Panepucci, R. R. & Lipson, M. Nanotaper for compact mode conversion. *Opt. Lett.* **28**, 1302–1304 (2003).
- [9] Almeida, V. R., Xu, Q., Barrios, C. A. & Lipson, M. Guiding and confining light in void nanostructure. *Opt. Lett.* **29**, 1209–1211 (2004).
- [10] Abbaslou, S., Gatlula, R., Lu, M., Stein, A. & Jiang, W. Ultra-short beam expander with segmented curvature control: the emergence of a semi-lens. *Opt. Lett.* **42**, 4383–4386 (2017).
- [11] Michaels, A. & Yablonovitch, E. Leveraging continuous material averaging for inverse electromagnetic design. *Opt. Express* **26**, 31717–31737 (2018).
- [12] Kawase, K., Ogawa, Y., Watanabe, Y. & Inoue, H. Non-destructive terahertz imaging of illicit drugs using spectral fingerprints. *Opt. Express* **11**, 2549–2554 (2003).
- [13] Guerboukha, H., Nallappan, K. & Skorobogatiy, M. Toward real-time terahertz imaging. *Adv. Opt. Photon.* **10**, 843–938 (2018).
- [14] Davies, A. G., Burnett, A. D., Fan, W., Linfield, E. H. & Cunningham, J. E. Terahertz spectroscopy of explosives and drugs. *Mater. Today* **11**, 18–26 (2008).
- [15] Baxter, J. B. & Guglietta, G. W. Terahertz spectroscopy. *Anal. Chem.* **83**, 4342–4368 (2011).
- [16] Nagatsuma, T., Ducournau, G. & Renaud, C. C. Advances in terahertz communications accelerated by photonics. *Nat. Photon.* **10**, 371 (2016).
- [17] Yu, X. *et al.* 160 Gbit/s photonics wireless transmission in the 300–500 GHz band. *APL Photonics* **1**, 081301 (2016).
- [18] Maxwell, J. C. & Niven, S. W. D. *The Scientific Papers of James Clerk Maxwell: Edited by WD Niven* (Dover Publications, 1890).

- [19] Gao, W. *et al.* Effective-medium-cladded dielectric waveguides for terahertz waves. *Opt. Express* **27**, 38721–38734 (2019).
- [20] Headland, D., Withayachumnankul, W., Yu, X., Fujita, M. & Nagatsuma, T. Unclad microphotonics for terahertz waveguides and systems. *J. Lightwave Technol.* **38**, 6853–6862 (2020).
- [21] Gao, W. J. *et al.* Characteristics of effective-medium-cladded dielectric waveguides. *IEEE Trans. Terahertz Sci. Tech.* (2020).
- [22] Tsuruda, K., Fujita, M. & Nagatsuma, T. Extremely low-loss terahertz waveguide based on silicon photonic-crystal slab. *Opt. Express* **23**, 31977–31990 (2015).
- [23] Hanham, S., Watts, C., Otter, W., Lucyszyn, S. & Klein, N. Dielectric measurements of nanoliter liquids with a photonic crystal resonator at terahertz frequencies. *Appl. Phys. Lett.* **107**, 032903 (2015).
- [24] Hanham, S. M., Ahmad, M. M., Lucyszyn, S. & Klein, N. LED-switchable high-Q packaged THz microbeam resonators. *IEEE Trans. Terahertz Sci. Tech.* **7**, 199–208 (2017).
- [25] Headland, D., Fujita, M. & Nagatsuma, T. Bragg-mirror suppression for enhanced bandwidth in terahertz photonic crystal waveguides. *IEEE J. Sel. Top. Quantum Electron.* **26**, 4900109 (2020).
- [26] Vincent, G. Optical properties of porous silicon superlattices. *Appl. Phys. Lett.* **64**, 2367–2369 (1994).
- [27] Diener, J. *et al.* Dichroic Bragg reflectors based on birefringent porous silicon. *Appl. Phys. Lett.* **78**, 3887–3889 (2001).
- [28] Union, I. ITU-T recommendation G.975.1. *Series G* (2004).
- [29] Swithenbank, M. *et al.* On-chip terahertz-frequency measurements of liquids. *Anal. Chem.* **89**, 7981–7987 (2017).
- [30] Nagai, M., Yada, H., Arikawa, T. & Tanaka, K. Terahertz time-domain attenuated total reflection spectroscopy in water and biological solution. *Int. j. Infrared millim. Waves* **27**, 505–515 (2006).
- [31] Zentgraf, T., Liu, Y., Mikkelsen, M. H., Valentine, J. & Zhang, X. Plasmonic Luneburg and Eaton lenses. *Nat. Nanotech.* **6**, 151–155 (2011).
- [32] Du, G., Liang, M., Sabory-Garcia, R. A., Liu, C. & Xin, H. 3-d printing implementation of an x-band eaton lens for beam deflection. *IEEE Antennas Wirel. Propag. Lett.* **15**, 1487–1490 (2016).
- [33] Sayanskiy, A. *et al.* Broadband 3-D Luneburg lenses based on metamaterials of radially diverging dielectric rods. *IEEE Antennas Wirel. Propag. Lett.* **16**, 1520–1523 (2017).
- [34] Valentine, J., Li, J., Zentgraf, T., Bartal, G. & Zhang, X. An optical cloak made of dielectrics. *Nat. Mater.* **8**, 568–571 (2009).
- [35] Gabrielli, L. H. & Lipson, M. Transformation optics on a silicon platform. *J. Opt.* **13**, 024010 (2010).
- [36] Liu, J., Mendis, R. & Mittleman, D. M. A Maxwell’s fish eye lens for the terahertz region. *Appl. Phys. Lett.* **103**, 031104 (2013).
- [37] Amarasinghe, Y., Mittleman, D. M. & Mendis, R. A Luneburg lens for the terahertz region. *J. Infrared Millim. Terahertz Waves* **40**, 1129–1136 (2019).
- [38] Sato, K. & Monnai, Y. Terahertz beam steering based on trajectory deflection in dielectric-free Luneburg lens. *IEEE Trans. Terahertz Sci. Tech.* **10**, 229–236 (2020).
- [39] Nagel, M., Marchewka, A. & Kurz, H. Low-index discontinuity terahertz waveguides. *Opt. Express* **14**, 9944–9954 (2006).
- [40] Amarloo, H. & Safavi-Naeini, S. Terahertz field localization using slot dielectric waveguide implemented in silicon-on-glass (SOG) technology. In *Proc. AN-TEM* (IEEE, 2018).
- [41] Aller, M. M. & Preu, S. Quasi-analytical description of a double slit planar dielectric waveguide as broadband dispersion compensating element. In *Proc. IRMMW-THz* (IEEE, 2019).
- [42] O’Brien, J. L., Furusawa, A. & Vučković, J. Photonic quantum technologies. *Nat. Photon.* **3**, 687–695 (2009).
- [43] Kutas, M. *et al.* Terahertz quantum sensing. *Sci. Adv.* **6**, eaaz8065 (2020).
- [44] Taha, M. *et al.* Insulator–metal transition in substrate-independent VO₂ thin film for phase-change devices. *Sci. Rep.* **7**, 17899 (2017).
- [45] Yu, X., Kim, J.-Y., Fujita, M. & Nagatsuma, T. Efficient mode converter to deep-subwavelength region with photonic-crystal waveguide platform for terahertz applications. *Opt. Express* **27**, 28707–28721 (2019).
- [46] Yu, X., Ohira, T., Kim, J.-Y., Fujita, M. & Nagatsuma, T. Waveguide-input resonant tunnelling diode mixer for THz communications. *Electron. Lett.* **56**, 342–344 (2020).
- [47] Subashiev, A. V. & Luryi, S. Modal control in semiconductor optical waveguides with uniaxially patterned layers. *J. Lightwave Technol.* **24**, 1513 (2006).